Energy & Environmental Science

Accepted Manuscript

This article can be cited before page numbers have been issued, to do this please use: L. Yang, Y. Shen, X. Long, Q. Ma, Z. Ruan, N. Xu, K. Li, L. Jiao, Y. Kong, J. Li, L. Tang, A. Yu and B. Cheng, *Energy Environ. Sci.*, 2025, DOI: 10.1039/D5EE01408E.

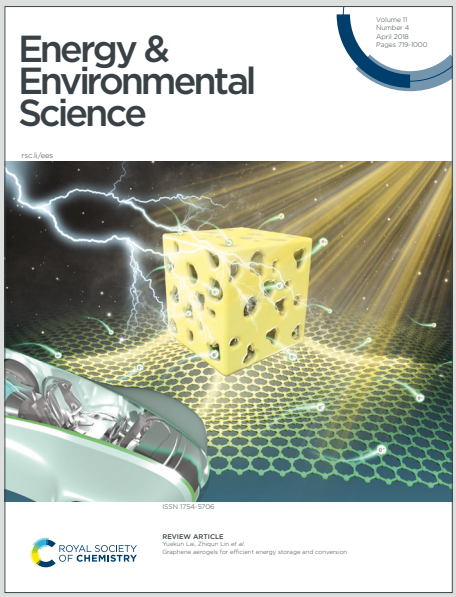

ROYAL SOCIETY OF CHEMISTRY

rsc.li/ees

View Article Online
DOI: 10.1039/D5EE01408E

The urgent need for sustainable, high-performance energy storage solutions drives innovation in aqueous zinc-ion batteries (AZIBs), which offer safety and scalability for grid applications. However, Zn anode instability, caused by dendrite growth and parasitic reactions, limits their practical viability under high-depth cycling. This study introduces a graphene oxide-reinforced poly(ether-block-amide) artificial SEI (P-G) that synergistically combines polymer functional groups and the electronegativity of GO to direct Zn^{2+} flux and suppress dendrites. As a result, P-G@Zn symmetric cells exhibit a record-breaking lifespan exceeding 5000 hours at 54.7% DOD and ultra-stable cycling for 6500 hours at 1 $mA \cdot cm^{-2}$. The P-G layer achieves a high Zn^{2+} transfer number (0.77) and rapid ion kinetics, enabling reversible Zn deposition. Additionally, a high-specific-energy P-G@Zn||I_2 pouch cell retains 82.8% capacity after 400 cycles with an N/P ratio of 2, validating practical feasibility. By integrating experimental and theoretical insights, this work bridges innovations developed in laboratory settings and practical AZIB deployment, establishing a universal framework for stabilizing metal anodes in next-generation batteries.

View Article Online
DOI: 10.1039/D5EE01408E

ARTICLE

Engineering ion-pumping solid electrolyte interphase for ultra-stable aqueous zinc-ion batteries under deep discharge conditions

Received 00th January 20xx,
Accepted 00th January 20xx

DOI: 10.1039/x0xx00000x

Leixin Yang,‡[*ab] Yujie Shen,‡[a] Xintao Long,‡[c] Qianyi Ma,[d] Ziqing Ruan,[a] Nuo Xu,[a] Kaihua Li,[a] Long Jiao,[a] Yaping Kong,[e] Jie Li,[a] Lei Tang[*f] Aiping Yu,[*d] and Bowen Cheng,[*a]

Meeting the global terawatt-scale energy demands necessitates innovative solutions to overcome the critical challenges facing aqueous Zn-ion batteries, particularly the poor reversibility and unstable plating/stripping of Zn anodes under high depths of discharge (DOD). In this work, we introduce a novel composite artificial solid-electrolyte interphase (SEI), termed P-G, which combines a poly(ether-block-amide) matrix with graphene oxide (GO). By leveraging the functional groups of the polymer (C=O, C–O–C) and the electronegativity of GO, the P-G SEI layer acts as a highly efficient Zn^{2+} ion pump, achieving a remarkable Zn^{2+} transfer number of 0.77 and fast ion transport kinetics. Comprehensive theoretical and experimental analyses demonstrate that the P-G SEI layer regulates Zn^{2+} coordination and forms rapid ion transport pathways, leading to a highly stable and reversible Zn anode. As a result, P-G@Zn symmetric cells achieve ultra-stable cycling for 6500 hours at 1 mA·cm^{-2} and a record-breaking lifespan exceeding 5000 hours at 54.7% DOD. Furthermore, a high-specific-energy P-G@Zn||I_2 pouch cell delivers exceptional performance, retaining 82.8% capacity after 400 cycles with an N/P ratio of 2. This study offers a compelling framework for designing advanced composite SEI layer, paving the way for highly reversible Zn-ion batteries in practical energy storage applications.

Introduction

The increasing global demand for sustainable energy and environmental stewardship has driven intense research into next-generation electrical energy storage (EES) systems powered by renewable and clean energy sources.[1, 2] Among these, aqueous zinc-ion batteries (AZIBs) have gained attention as a promising solution for grid-scale energy storage due to their high theoretical capacity (820 mAh·g^{-1} or 5854 mAh·cm^{-3}), low redox potential (-0.76 V vs. SHE), intrinsic safety, and low cost. However, despite these advantages, the widespread adoption of AZIBs is hindered by critical challenges associated with the reversibility and stability of zinc (Zn) metal anodes, particularly under high depths of discharge (DOD). Issues such as hydrogen evolution reactions (HER), corrosion reaction, and dendrite formation lead to low coulombic efficiency and poor cycle life,[3-5] stemming from the thermodynamic instability of Zn metal in neutral or mildly acidic electrolytes.[6-8]

A fundamental limitation of AZIBs compared to lithium-ion batteries (LIBs) is their inability to naturally form a robust solid electrolyte interphase (SEI) layer, which is crucial for mitigating challenges. [9] To overcome these barriers, researchers have explored a range of strategies, including advanced electrode structure designs, electrolyte optimization, separator modifications, and protective layer engineering.[10-12] Among these approaches, constructing protective layers is particularly promising as it enables the direct formation of functional SEI layers on Zn anodes via in-situ generation or ex-situ

a State Key Laboratory of Bio-based Fiber Materials, Tianjin Key Laboratory of Pulp and Paper, China Textile Industry Key Laboratory of High-performance Fibers Wet-laid Nonwoven Materials, Tianjin University of Science and Technology, Tianjin 300457, China
b Wanli Energy Technology Development Co., Ltd, Institute of Carbon Neutrality, Zhejiang Wanli University, Ningbo 315100, China
c Guangdong Provincial Key Laboratory of Nanophotonic Functional Materials and Devices, School of Information and Optoelectronic Science and Engineering, South China Normal University, Guangzhou 510006, China
d Department of Chemical Engineering, Waterloo Institute for Nanotechnology, University of Waterloo, Waterloo, ON, N2L3G1, Canada
e Vacuum Interconnected Nanotech Workstation, SINANO, CAS, Suzhou 215123, China;
*f Institute of Sustainability for Chemicals, Energy and Environment (ISCE2), Agency for Science, Technology and Research (A*STAR), 1 Pesek Road, Singapore, 627833 Republic of Singapore*.
Supplementary Information available: [details of any supplementary information available should be included here]. See DOI: 10.1039/x0xx00000x

View Article Online
DOI: 10.1039/D5EE01403F

coating.[13] Polymer-based artificial SEI layers are especially attractive due to their excellent interfacial affinity and tunable functional groups. However, achieving mechanically and chemically stable polymer layers in aqueous environments remains a formidable challenge, as they must also minimize interfacial resistance and maintain efficient ion transport.

In this regard, two-dimensional (2D) materials have emerged as transformative components in protective coatings. Their atomic-scale thickness, exceptional mechanical strength, and unique electrochemical properties make them ideal for addressing the limitations of Zn anodes. Recent studies combining polymers with 2D materials have demonstrated significant progress in enhancing cycling stability.[14-16] For example, hybrid layers incorporating 2D $Ti_3C_2T_x$ nanosheets or 2D metal-organic frameworks have shown excellent reversibility and improved Zn^{2+} transport.[17] Despite these breakthroughs, current solutions are mainly effective at low DOD (below 50%), as the Zn anode suffers from more severe structural degradation and side reactions under high DOD. Therefore, developing SEI coatings that enable uniform electric field distribution and stable Zn^{2+} plating/stripping at high DOD is essential-but highly challenging - for AZIBs toward large scale applications.[18, 19]

Drawing inspiration from biological ion pumps—such as ATPase proteins that mediate Na^+/K^+ transport across cell membranes by leveraging coordination interactions to drive active ion movement against concentration gradients—we introduce a biomimetic 'ion pumping' concept for advanced solid-electrolyte interphase design. [20] In this work, we address this by designing a hybrid SEI layer (P-G) comprising a poly(ether-block-amide) polymer and graphene oxide (GO), forming a hydrogen-bond-linked network with an ion-pumping effect (**Fig. 1a**). The P-G SEI layer enhances bonding strength and facilitates rapid Zn^{2+} transport on the Zn surface (P-G@Zn). The electronegativity of GO induces selective Zn^{2+} transport, enabling uniform, dendrite-free Zn deposition. The functional groups (C=O, C–O–C) of the P-G SEI layer regulate the Zn^{2+} solvation structure and electrolyte concentration, suppressing HER and by-product formation. As a result, the P-G SEI layer achieves exceptional electrochemical performance. Symmetric cells exhibit an ultra-long lifespan of 6500 hours at 1 mA·cm^{-2} and stable cycling over 5000 hours at 54.7% DOD. Additionally, Zn||I_2 full cells show superior capacity retention of 95.5% over 36,000 cycles and excellent cycling stability in pouch cells at high specific energy and Zn DOD. This work offers new insights into designing advanced SEI layers, paving the way for the practical application of AZIBs in next-generation energy storage systems.

Results and discussion

Construction and characterization of P-G

Graphene oxide (GO), a prominent two-dimensional material, boasts excellent conductivity, an ultrahigh specific surface area, and superior mechanical strength.[21] These properties make it a suitable candidate for dispersing current density, restricting lateral diffusion of Zn^{2+}, and promoting uniform deposition. The foundational characteristics of the GO employed throughout this work are summarized in **Table S1**, with corresponding experimental testing protocols detailed in **Fig. S1** and **S2**. However, when applied as SEI layer for zinc anodes, GO faces challenges. Its weak bonding with zinc, caused by van der Waals forces between layers, leads to poor structural stability. Consequently, GO tends to restack on the surface, making complete coverage difficult (**Fig. S3**). Additionally, as shown in **Fig. S4**, GO tends to peel off during the bending of zinc foil.

To address these limitations, poly(ether-block-amide) (PEBA) was chosen to enhance the bonding between the SEI layer and zinc metal. PEBA, a multifunctional polymer, was dissolved into a homogeneous solution, blended with GO, and drop-cast onto the zinc foil surface (**Fig. S5**).[22] The drop-casting method offers simplicity and low cost, making it advantageous compared to other preparation techniques. The structure of PEBA includes hydrophilic C-O-C groups in the PEO chain segment and zincophilic -CO-NH- groups in the PA chain segment (**Fig. S6**), contributing to its multifunctionality.[23]

The composite material, termed P-G, was characterized using Fourier-transform infrared spectroscopy (FTIR). As shown in **Fig. 1b** and **Fig. S7**, GO exhibits peaks at 1640 cm^{-1}, attributed to the stretching vibration of C=O in carboxyl groups, and a broad peak 3300 cm^{-1}, corresponding to O-H vibrations. PEBA displays characteristic peaks related to N-C=O and -O- groups.[24] In the P-G SEI layer, the presence of both types of characteristic peaks, along with shifts in the C=O peak, confirms the formation of hydrogen bonds between GO and PEBA.

Mechanical testing further highlights the advantages of the composite material. Films of PEBA and P-G, prepared on a PTFE substrate via tape casting, were subjected to tensile tests (**Fig. 1c**). The PEBA film demonstrated excellent mechanical strength due to the rigid PEO segments, while the addition of hydrogen bonds in the composite film significantly enhanced its performance, allowing it to withstand tensile forces of nearly 20 MPa. Remarkably, the P-G film exhibited exceptional flexibility in wet environments, with an elongation at break exceeding 1100% (**Fig. S8**). Additionally, the puncture resistance of the P-G SEI layer was three times that of pure PEBA film (**Fig. S9**), ensuring sufficient mechanical properties to accommodate volume changes and resist dendritic punctures during zinc plating/stripping cycles (**Fig. 1d**).

To optimize the P-G SEI layer's thickness and polarization voltage, the amount of drop-coating solution was adjusted, with 45 μL yielding the best electrical performance and cycle life (**Fig. S10**). As shown in **Fig. S11**, systematic modulation of GO concentration revealed a direct correlation with electrochemical performance, where the optimized loading of 1.0 mg·cm^{-2} delivered superior cycling stability. Zeta potential measurements show that the surface potential of GO is -40.1 mV (**Fig. 1e**), primarily due to its abundant oxygen-containing functional groups, such as carboxyl (-COOH) and hydroxyl (-OH). The negatively charged GO imparts electronegativity to the P-G surface, enhancing its attraction to Zn^{2+} ions while repelling anions.[25] Scanning electron microscopy (SEM) images (**Fig. 1f**) reveal a dense and uniform 10 μm thick protective layer on the zinc surface, where

View Article Online
DOI: 10.1039/D5EE01408E

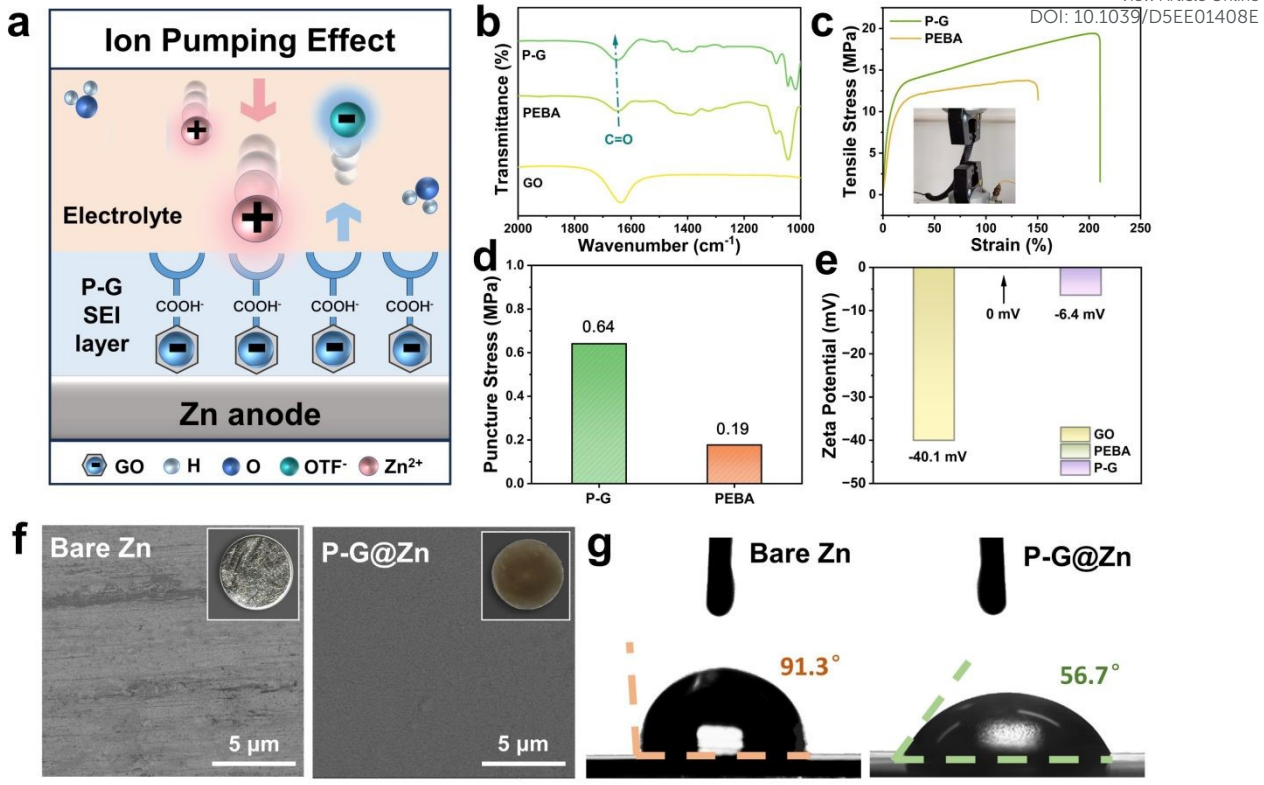

Fig. 1. Structural characterizations of the P-G SEI layer. (a) The schematic diagram of regulating mechanism of ion pump in P-G SEI layer. (b) Partial magnification of FTIR spectra of GO, PEBA and P-G. (c) Elongation at break of PEBA and P-G films after drying. (d) Mechanical property of PEBA and P-G films. (e) Zeta potential of GO, PEBA and P-G. (f) Optical images and SEM images of bare Zn foil and P-G@Zn foil. (g) Contact angles of 3 M OTF aqueous solution on the bare Zn foil and P-G@Zn foil.

nano-sized GO is tightly anchored in the PEBA matrix. Energy-dispersive spectroscopy (EDS) analysis (**Fig. S13**) confirms the uniform distribution of C and O elements on the surface, with no visible zinc underneath, indicating complete coverage. Even after repeated folding of the zinc foil, the protective layer remained intact, highlighting its durability and effectiveness in long-term cycling (**Fig. S15**).

The wettability of the protective layer was also evaluated using contact angle tests with a 3M $Zn(OTf)_2$ electrolyte. While the contact angle on bare zinc was 91.3°, it significantly decreased to 56.7° on the P-G SEI layer surface (**Fig. 1g**). This improved wettability, attributed to the abundant hydroxyl groups and ether oxygen bonds in the P-G SEI layer, enhances the solvation structure of Zn^{2+} and facilitates the diffusion of water molecules on the surface, further supporting its role in stabilizing zinc anodes.[19]

Characterization of anti-corrosion capability

Continuous interface corrosion between the electrode and electrolyte in assembled cells leads to the formation of by-products and hydrogen evolution reactions, significantly limiting the performance of AZIBs.[26] To evaluate the corrosion resistance of the P-G SEI layer, zinc plates with and without coatings were immersed in electrolytes. As shown in **Fig. 2a**, after five days of soaking, the surface of the bare zinc plate exhibited large dendrites and blocky by-products, as revealed by SEM images. In contrast, the zinc plate with the P-G SEI layer showed minimal corrosion after the coating was removed. XRD analysis of the surface-passivated zinc foil revealed distinct peaks at 6.6°, 13.1°, 19.8°, and 31.2°, indicating corrosion on the zinc surface in the absence of P–G protection and decomposition of $(OTf)^-$ anions (**Fig. 2b**). This demonstrates that the protective layer effectively prevents corrosion. Additional SEM observations (**Fig. S16**) revealed that the P-G SEI layer forms a flawless coating on the zinc plate, maintaining excellent corrosion protection even after 14 days of electrolyte immersion, as evidenced by the absence of dendrites and significant by-product peaks (**Fig. S17**).

To assess the thermodynamic stability of the P-G SEI layer, corrosion current density measurements were performed. As shown in **Fig. 2c**, the corrosion current density of bare zinc in the electrolyte was 19.6 mA cm^{-2}, significantly higher than that of P-G@Zn (5.1 mA cm^{-2}). Moreover, the coated zinc foil exhibited an increase in corrosion potential, indicating enhanced anti-corrosion performance. These results demonstrate the positive effect of the P-G SEI layer on improving the corrosion resistance of the zinc metal anode.

The effectiveness of the P-G SEI layer in suppressing the hydrogen evolution reaction (HER) was evaluated through linear sweep voltammetry (LSV) in a three-electrode system. To avoid interference from zinc deposition, 1M Na_2SO_4 was used as the electrolyte. In this setup, the zinc foil served as the working electrode, Pt foil as the

View Article Online
DOI: 10.1039/D5EE01408E

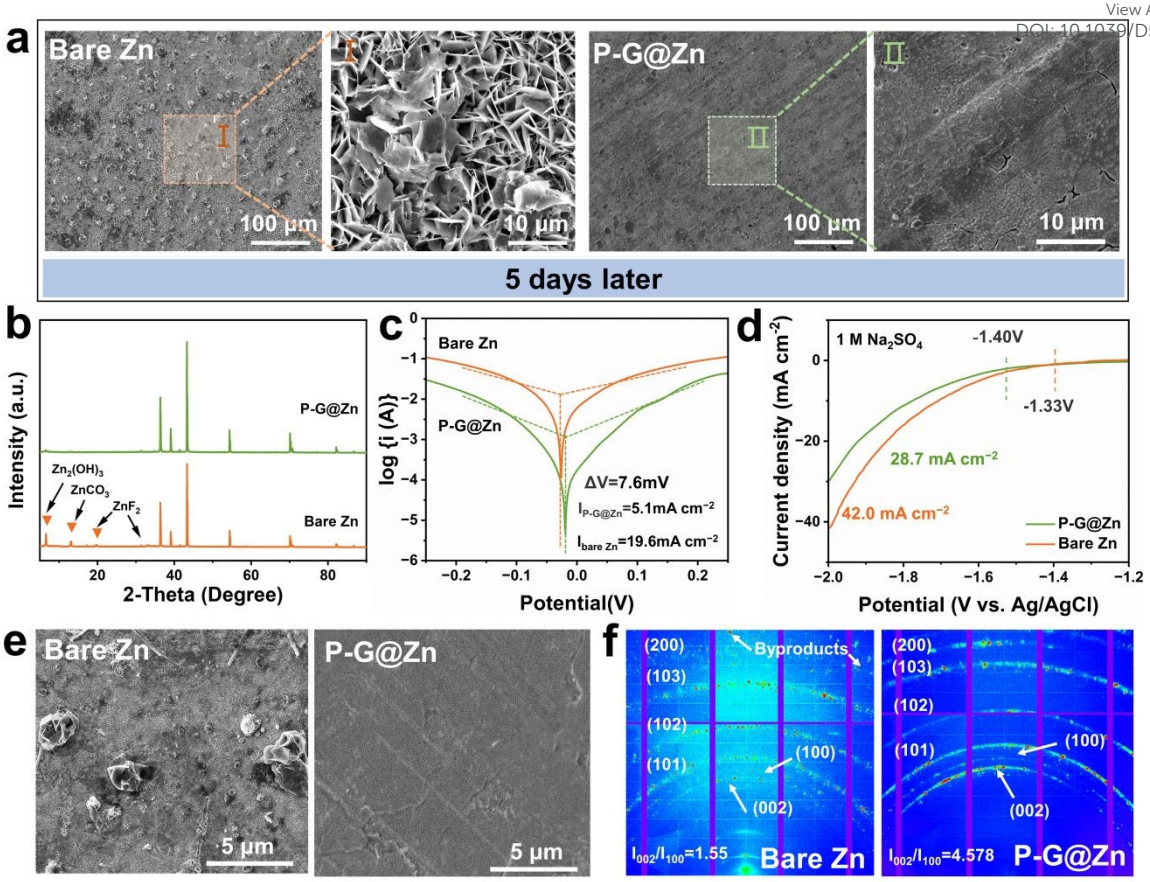

Fig. 2. Anti-corrosion performance of P-G@Zn anode. (a) Surface SEM images of bare Zn and P-G@Zn immersed in electrolyte after 5 days. (b) XRD patterns of bare Zn and P-G@Zn soaked in electrolyte after 5 days. (c) Tafel curves of bare Zn and P-G@Zn. (d) LSV curves of bare Zn and P-G@Zn. (e) SEM images of bare Zn and P-G@Zn after removing the P-G layer after cycling 60 h at 1 mA cm^{-2}. (f) WAXS patterns for cycled bare Zn and cycled P-G@Zn.

counter electrode, and Ag/AgCl as the reference electrode.[27] As shown in **Fig. 2d**, the P-G SEI layer reduced the cathodic current density from 42.0 mA·cm^{-2} to 28.7 mA·cm^{-2}, accompanied by a larger polarization potential. Optical images revealed a significant number of bubbles on the bare zinc anode surface during the test, whereas no bubbles were observed on the P-G SEI layer surface. This directly confirms that the protective layer suppresses HER, consistent with the test data (**Fig. S20**). A lower corrosion current density and more positive corrosion potential typically signify superior corrosion resistance.[28]

The excellent corrosion resistance of the P-G SEI layer contributes to a dendrite-free anode during cycling. To further investigate this, symmetrical cells were cycled at 1 mA·cm^{-2} (1 mAh·cm^{-2}) for 30 cycles. While dendritic structures were observed on the bare zinc anode after cycling, the P-G@Zn||P-G@Zn cell exhibited a smooth anode surface (**Fig. 2e**). XRD patterns of the uncoated and coated anodes revealed differences in the peak intensity ratio of the (002) plane to the (100) plane (**Fig. S21**). The ratio for the P-G@Zn anode was 4.578, significantly higher than the 1.55 observed for the bare Zn anode. The dominance of the Zn (002) plane, characterized by lower surface energy and higher stability, supports uniform horizontal deposition of zinc ions and inhibits dendrite formation. Further insights into the crystal structure changes after cycling were obtained using two-dimensional wide-angle X-ray scattering (WAXS) patterns (**Fig. 2f**). The bare zinc anode displayed chaotic diffraction peaks and significant by-product diffraction peaks, which were almost absent on the P-G SEI layer.[29] This indicates that the zinc deposits on the bare surface were random and irregular, leading to severe tip discharge effects and exacerbating dendrite growth.[30] In summary, the P-G SEI layer demonstrates excellent thermodynamic and kinetic stability. Its superior wettability captures water molecules and homogenizes the surface electrolyte, effectively shielding the zinc anode from direct contact with the electrolyte. As a result, the P-G SEI layer prevents corrosion, suppresses hydrogen evolution reactions, and minimizes by-product formation, ensuring long-term stability and performance for AZIBs.

Characterization of deposition behavior

To investigate the influence of the ion pump effect from the P-G SEI layer on zinc deposition behavior, chronoamperometry (CA) was conducted to analyze the zinc ion growth mechanism on the anode (**Fig. 3a**). The current variation was monitored over 150 seconds under a constant potential of 150 mV. For the bare zinc electrode, the current density increased continuously, indicating rampant two-

dimensional diffusion on the anode surface. This uncontrolled diffusion leads to uneven zinc deposition, where the severe tip effect promotes dendritic growth. Such dendrites can puncture the separator, potentially causing battery short circuits.[31] In contrast, with the P-G SEI layer, the current curve stabilized within 30 seconds and ceased decreasing, suggesting the system quickly transitioned to stable three-dimensional diffusion. This behavior enables uniform zinc ion deposition on the anode surface, ultimately forming Zn^0.[32]

In addition, a zinc-copper cell is constructed and the nucleation potential of zinc is assessed through cyclic voltammetry (CV) testing, as depicted in **Fig. 3b**. The uniform deposition of Zn^{2+} is largely attributed to the initial nucleation behavior. Point A represents the potential intersection of the CV curves, while point B/B' indicates the onset of zinc ion reduction on the copper anode surface. The potential difference between these points, termed the nucleation overpotential, is a critical factor. On the P-G SEI layer surface, the presence of abundant polar groups with strong coordination capabilities prevents uncontrolled zinc ion diffusion and increases the deposition potential. This is reflected in the CV results, where the nucleation overpotential of P-G@Zn is higher than that of the bare zinc-copper cell (66 mV).[33] It is worth noting that although the nucleation overpotential of the coated anode is higher than that of the control, classical nucleation theory suggests that this promotes a higher nucleation site density, leading to more uniform Zn deposition with finer particle size. The increased overpotential also provides a stronger thermodynamic driving force for the formation and growth of finer Zn nuclei.

The ion pump effect of the P-G SEI layer facilitates Zn^{2+} transport, expediting zinc deposition. This mechanism helps maintain a stable potential difference on the electrode surface, preventing random migration and aggregation of zinc ions and ensuring uniform deposition. As shown in **Fig. S22**, the morphology of zinc deposited on the copper surface at a current density of 0.5 $mA \cdot cm^{-2}$ reveals a porous zinc coating in the bare Zn||Cu semi-symmetric cell. In contrast, the P-G SEI layer exhibits a denser galvanized layer. Similarly, **Fig. S23** highlights significant differences in the zinc anode surfaces, further demonstrating the impact of it.

The nucleation behavior of zinc ions can also be modulated by regulating the solvation structure of Zn^{2+} through the protective layer. During the electroplating process, Zn^{2+} must overcome the desolvation energy barrier from $[Zn(H_2O)_6]^{2+}$.[34] A high energy barrier slows zinc ion migration, leading to significant concentration and potential differences between the zinc anode and electrolyte, which adversely affect battery reversibility.[35] As shown in **Fig. S24**, the charge transfer resistance (R_{ct}) of Zn@P-G is lower than that of bare Zn cell at the same temperature, indicating enhanced anode migration kinetics after coating.[3] FTIR results (**Fig. S25** and **S26**) reveal a redshift in the characteristic bands of C–O–C and C=O, confirming chemical interactions between Zn^{2+} and the P-G SEI layer. The activation energy (E_a) is obtained using the Arrhenius equation to investigate and evaluate the desolvation capability of zinc anode with/without P-G. **Fig. 3c** illustrates that the P-G@Zn anode reveals a smaller E_a of 30.4 KJ mol^{-1} in comparison with the bare Zn anode (42.9 KJ mol^{-1}). And this demonstrates that the P-G SEI layer can accelerate the Zn^{2+} desolvation process and facilitate ion migration kinetics.

The uniform and dense the P-G SEI layer also facilitates the dissociation of water molecules in hydrated zinc ions. The Zn-ion transfer number (t_{Zn2+}) is measured to evaluate the migration speed of zinc ions (**Fig. 3d** and **S27**). Compared with the initial interfacial resistance of bare zinc, the initial interfacial resistance of P-G@Zn increases to a certain extent due to the introduction of polymer coating. The increase in resistance of bare zinc is observed to be significantly higher compared to the resistance exhibited by the P-G SEI layer. Calculations show that the t_{Zn2+} values for bare zinc and P-G@Zn are 0.29 and 0.77, respectively. It is worth noting that although the Zn^{2+} transference number reflects the bulk properties of the electrolyte, the anode coating can indirectly influence the measured value by: (i) inhibiting side reactions that alter the bulk composition; (ii) stabilizing the electrode–electrolyte interface; and (iii) affecting the interfacial concentration profile and polarization behavior involved in the measurement process. As shown in **Fig. 3e**, it is found that the ionic conductivity about 42.91 mS cm^{-1} was achieved for the P-G@Zn, which represents the total impedance of the cell and indicates the effective conductivity of the full interfacial configuration. The ionic conductivity of the free-standing P-G SEI layer is measured at 31.05 mS cm^{-1} **(Fig. S28)**, which indicates that the construction of the P-G SEI layer serves as an effective strategy to enhance the migration rate of zinc ions at P-G@Zn interface. These findings demonstrate that constructing the P-G SEI layer is an effective strategy to enhance the zinc-ion migration rate.

X-ray photoelectron spectroscopy (XPS) and focused ion beam scanning electron microscopy (FIB-SEM) analyses are conducted to investigate the surface reactions and morphology of the zinc anode after cycling.[36, 37] As shown in **Fig. 3f** and **S29**, the O 1s peaks at 532.2 eV and 530.5 eV correspond to C–O and C=O bonds, respectively, while the N 1s peak at 398.2 eV, attributed to N–Zn bonds, is absent in the bare zinc electrode. This finding indicates that the artificial SEI participates in Zn^{2+} desolvation and effectively regulates its diffusion behavior.[38] FIB-SEM images reveal significant surface irregularities and inconsistent zinc deposition with voids and cracks on the cycled bare Zn, whereas the removal of the P-G SEI layer exposes a uniform and void-free zinc surface (**Fig. 3g** and **S30**). The 3D reconstruction images (**Fig. 3h**) further show that the maximum surface height of cycled Zn (6.82 μm) is three times greater than that of P-G@Zn (1.90 μm), with the latter exhibiting a much smoother surface, as indicated by surface roughness analysis.[39] These results demonstrate that the P-G SEI layer provides abundant adsorption sites for zinc ions and nano-ion channels, which are anticipated to significantly enhance the cycling performance of AZIBs.

View Article Online
DOI: 10.1039/D5EE01408E

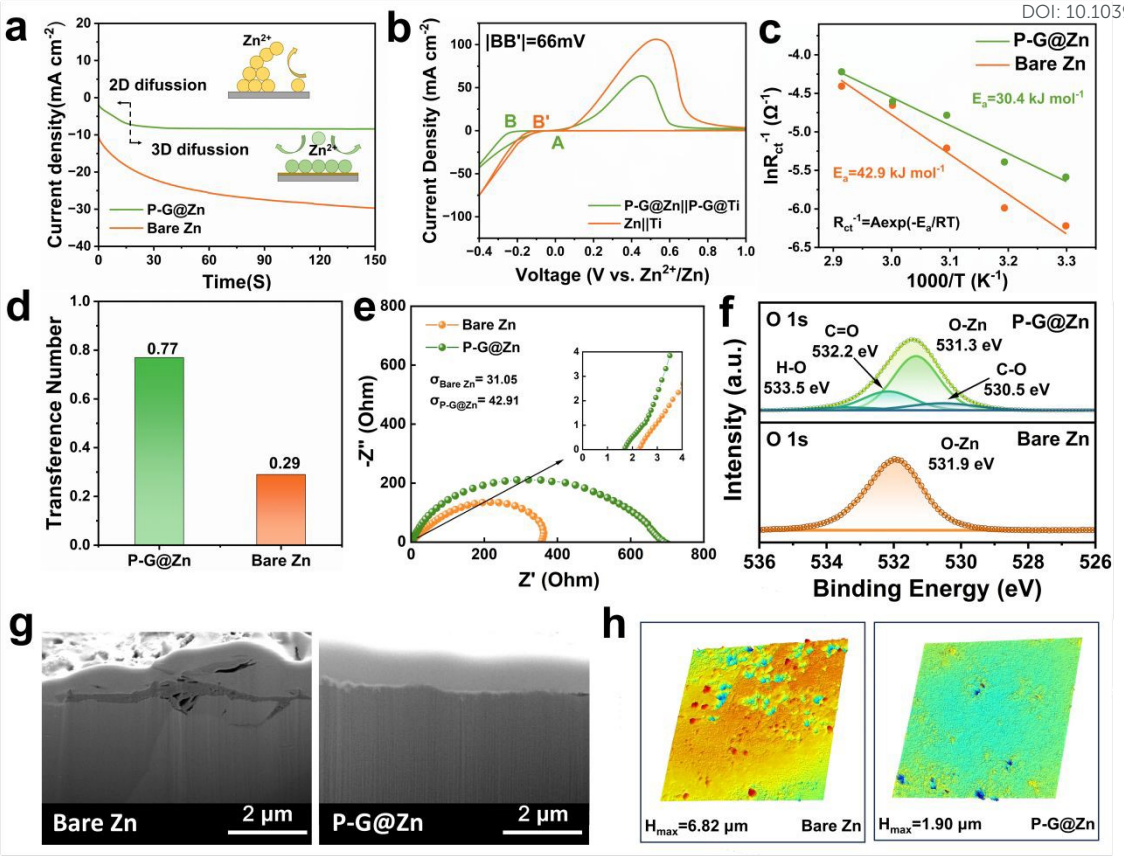

Fig. 3. Regulation of Zn^{2+} deposition behavior of the P-G SEI layer. (a) CA curves at -150 mV overpotential. (b) CV curves. (c) Arrhenius curves. (d) Zn^{2+} transference numbers of bare Zn and P-G@Zn symmetric cells. (e) Ionic conductivity (unit: mS cm^{-1}). (f) XPS spectras of O 1s. (g) Cross-section SEM images of cycled anodes post FIB etching. (h) Surface roughness of cycled anodes after 30 cycles (1 mA cm^{-2}, 1 mA h cm^{-2}).

Mechanisms of P-G SEI layer in regulating Zn deposition

The artificial SEI layer effectively mitigates issues such as dendrite formation and side reactions observed on the bare zinc anode through multiple protective mechanisms (**Fig. 4a**). On the rough and defective surface of the bare zinc anode, uneven Zn^{2+} concentration distribution between the electrolyte and metal surface leads to random deposition of Zn^{2+} at regions with high tip potential, triggering the tip effect.[40] This results in dendrite formation and "dead zinc," which negatively impacts the cycle performance of AZIBs. Additionally, the desolvation process releases H_2O, which undergoes HER on the metal surface, releasing H^+ ions and altering the cell's pH. This in turn initiates corrosion and generates by-products that further disturb the electric field distribution, increasing cell impedance.[41] The P-G SEI layer, with its excellent surface wettability and abundant functional groups, accelerates the dissolution process of Zn^{2+}. Critically, this induces an 'ion pump effect' driven by the strong coordination affinity between the artificial SEI layer and Zn^{2+}, enabling their active transport against concentration gradients and promoting directional acceleration at the anode interface. The uniformly distributed GO on the zinc surface forms ion transport channels, facilitating the rapid in-situ deposition of Zn^{2+}.[42, 43]

The adsorption behavior of Zn^{2+} at various sites on the anode surface can be further investigated to elucidate Zn^{2+} migration kinetics using density functional theory (DFT) simulations (**Fig. 4b**).[44, 45] The binding energy of Zn^{2+}-$6H_2O$ is significantly weaker than the adsorption strength of Zn^{2+} at various active sites in P-G SEI layer, as shown in **Fig. S31** and **S32**. In particular, the binding energy of Zn^{2+}-O atom (-1.38 eV) in GO (C=OOH) is the highest, confirming that the ion pump effect in P-G SEI layer facilitates the desolvation process of Zn^{2+} and guides uniform Zn^{2+} flux. For the sake of comparing the difference of Zn^{2+} surface concentration distribution caused by Zn dendrite growth with or without the P-G SEI layer, modeling and finite element analysis are carried out by COMSOL software (**Fig. S33**).[37, 46] As illustrated in **Fig. 4c** and **S34**, while Zn^{2+} accumulates at dendritic sites on bare Zn, the P-G SEI layer demonstrates homogeneous Zn^{2+} deposition via directional ion pumping.

XAFS analysis is utilized to simulate the Zn^{2+} solvation structure on the P-G SEI layer surface and in 3 M OTF electrolyte. In the X-ray absorption near edge structure (XANES) spectrums, zinc foil exhibits the lowest leading edge peak energy, indicative of Zn^0 (**Fig. 4d**).[47] In contrast, P-G/OTF demonstrates a moderate edge peak energy,

suggesting that the valence state of Zn in P-G SEI layer is lower than that in the OTF electrolyte.[48] The shift of the absorption edge towards lower energy indicates an increased electron density surrounding Zn^{2+}. This alteration in valence state arises from the negatively charged GO in P-G SEI layer acting as an electron donor, thereby modulating the solvation structure of Zn^{2+}. As illustrated in the **Fig. 4e**, the predominant single-coordination shell at approximately 1.8 Å is attributed to Zn-O interactions, while the peak observed near 1 Å results from low-frequency noise generated during testing. The presence of P-G SEI layer leads to a reduction in the radial distance of Zn-O (from 1.63 Å to 1.59 Å), indicating an enhanced interaction between P-G SEI layer and Zn^{2+}. This modification facilitates the dissolution of Zn^{2+} at the electrolytic electrode interface during deposition.[49, 50] The findings demonstrate that P-G SEI layer effectively optimizes the solvation structure of Zn^{2+}. To visualize the deposition process of Zn^{2+}, we monitored the deposition of Zn^{2+} using an in-situ optical microscope under high current conditions of 10 mA·cm^{-2}. Within 30 minutes, large uneven zinc deposits appeared on the surface of the bare Zn, accompanied by the formation of visible grey by-products and bubble formation. On the contrary, Zn^{2+} on the surface of the P-G@Zn deposited more finely and uniformly (**Fig. 4f**). In addition, the nanoindentation tests was conducted to analyze the formation of dendrite anodes from a physical perspective (**Fig. S35**). The P-G SEI layer shows a low hardness and small elastic modulus (Er) value of 0.33 GPa, which is significantly smaller than the cycled P-G@Zn anode (remove P-G SEI layer) of 24.1 GPa. This phenomenon is mainly attributed to the fact that the P-G layer facilitates the formation of a dendrite-free anode by ensuring a uniform zinc ion flux, instead of suppressing dendrite formation through a physical mechanism.

Electrochemical stability and reversibility of Zn electrodes

The plating/stripping performance of zinc anode is evaluated through constant current long-term cycle of symmetrical and asymmetric cells.[51-53] At a current density of 1 mA·cm^{-2}, bare Zn||Zn symmetric cells experienced short circuits after just 140 hours, likely due to hydrogen evolution reactions (HER) and uncontrolled dendrite growth (**Fig. 5a**). In contrast, P-G@Zn||P-G@Zn cells exhibited remarkable electrochemical performance, maintaining stable cycling

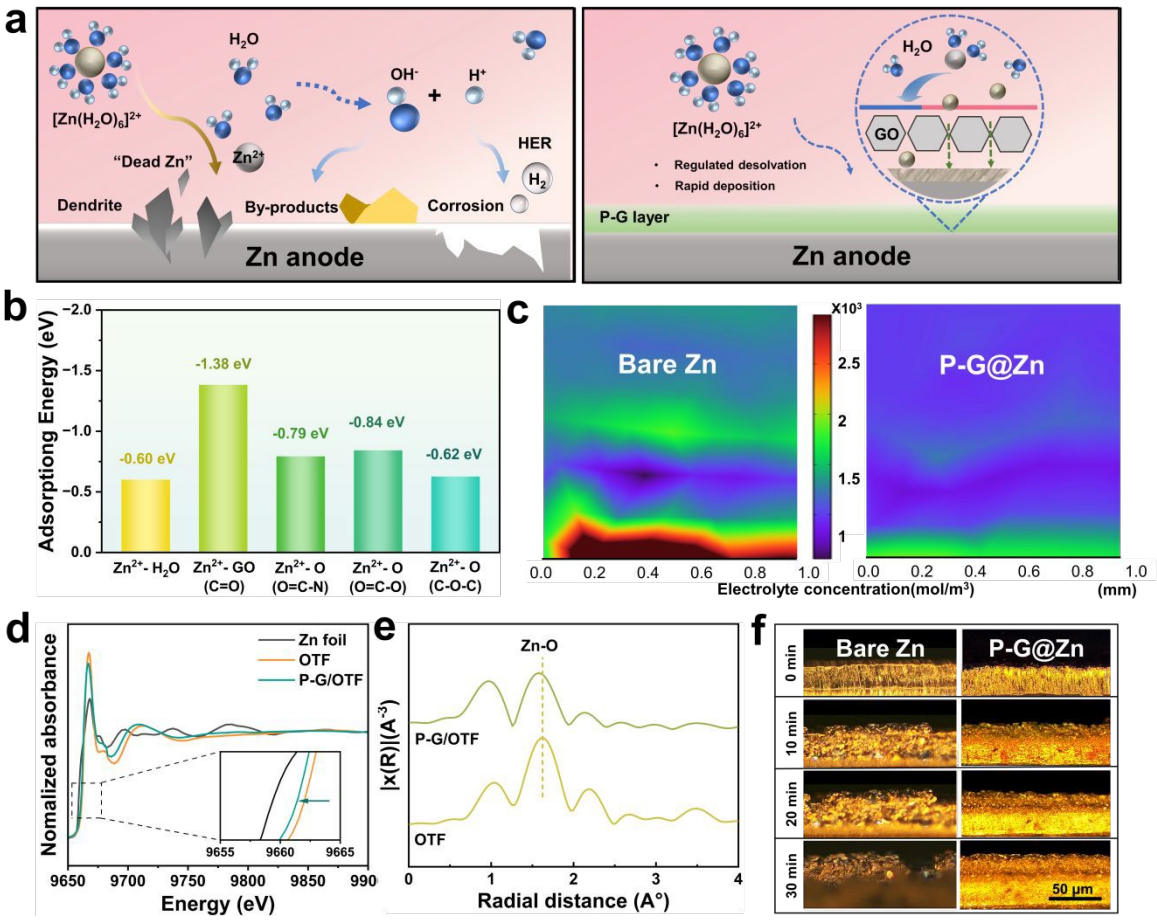

Fig. 4. Mechanisms of P-G SEI layer on regulating Zn deposition. (a) Schematic diagram illustrating the effect of the P-G SEI layer in the highly reversible zinc anodes. (b) Corresponding binding energies of Zn^{2+} with different ligands. (c) Simulation results of electrolyte concentration distribution on bare Zn and P-G@Zn surface. (d) Zn K-edge XANES spectra of Zn foil, OTF electrolyte, and P-G/OTF electrolyte. (e) Fourier transformed extended X-ray absorption fine structure (FT-EXAFS) in R space. (f) In situ microscopic images of bare Zn and P-G@Zn surface following 0, 10, 20, 30 min treatments at 10 mA cm^{-2}.

for up to 6600 hours. Post-cycling analysis revealed a significant thickness increase in the bare Zn cell, attributed to HER during electrolyte immersion, leading to anode degradation and electrolyte consumption (**Fig. S36**). It is worth noting that the polarization voltage of the P-G@Zn cell remained stable over 6000 hours, even as the current density increased from 1 to 20 mA·cm^{-2}. This indicates the P-G SEI layer's adaptability to high currents and its durability under fast charging and discharging conditions. In contrast, bare Zn symmetric cells showed irregular polarization curves and rapid deactivation at higher current densities (**Fig. 5b**).

Coulombic efficiency (CE), a critical parameter for evaluating electrode reversibility, is determined by the ratio of zinc stripped and deposited during a cell cycle.[54, 55] In addition to zinc loss from uneven deposition/stripping, the HER and byproduct formation also consume zinc ions and contribute to reduced CE. As shown in **Fig. 5c**, the bare Cu||Zn cell exhibits only 160 cycles at a current density of 1 mA·cm^{-2}, with significant fluctuations in CE. In contrast, the P-G@Cu||P-G@Zn cell achieves an average CE of 99.2% under the same conditions, maintaining a stable cycle life of 1000 cycles (**Fig. S37**). At higher current density and capacity (10 mA cm^{-2},10 mA h cm^{-2}), P-G@Zn demonstrates exceptional durability, achieving a cycle life of 1500 hours (**Fig. 5d**). To assess its practical potential, the Zn||Zn cell underwent a rigorous deep discharge test (**Fig. 5e**). The bare Zn||Zn cell deactivated after just four cycles (**Fig. S38**), whereas the P-G@Zn||P-G@Zn cell exhibited remarkable stability, sustaining a cycle life of 5000 hours-approximately 78 times longer. Even under extreme discharge depths (DOD$_{Zn}$ = 68.32% and 88.82%), P-G@Zn maintained cycling stability of over 700 and 500 hours, respectively (**Fig. S39** and **S40**). Performance comparison graphs (**Fig. 5f** and **5g**) further highlight the superior cycling stability of P-G@Zn. Existing studies typically use zinc plates over 100 μm thick to enhance electrical stability.[19] However, limited zinc utilization remains a major obstacle to the widespread application of AZIBs. The P-G SEI layer significantly improves electrochemical stability and enables prolonged cycling under high discharge depths, outperforming similar studies. These results present a promising strategy for advancing the commercial viability of aqueous zinc batteries.

The practical application potential of P-G@Zn was further validated using two distinct cathodes: V_2O_5 and I_2. At a scan rate of 1 mV s^{-1}, the cyclic voltammogram (CV) profiles of the Zn||V_2O_5 cells manifested two pairs of redox peaks.[16, 56] Critically, the P-G SEI layer, which suppresses interfacial side reactions and accelerates Zn^{2+} transport, optimizes ion migration dynamics, therefore reduces the voltage gap between the oxidation and reduction, and enhances reaction reversibility (**Fig. 6a**). Coupled with the reduced impedance of the full cells protected by the coating, these findings verify that the P-G SEI layer promotes faster reaction kinetics and minimizes

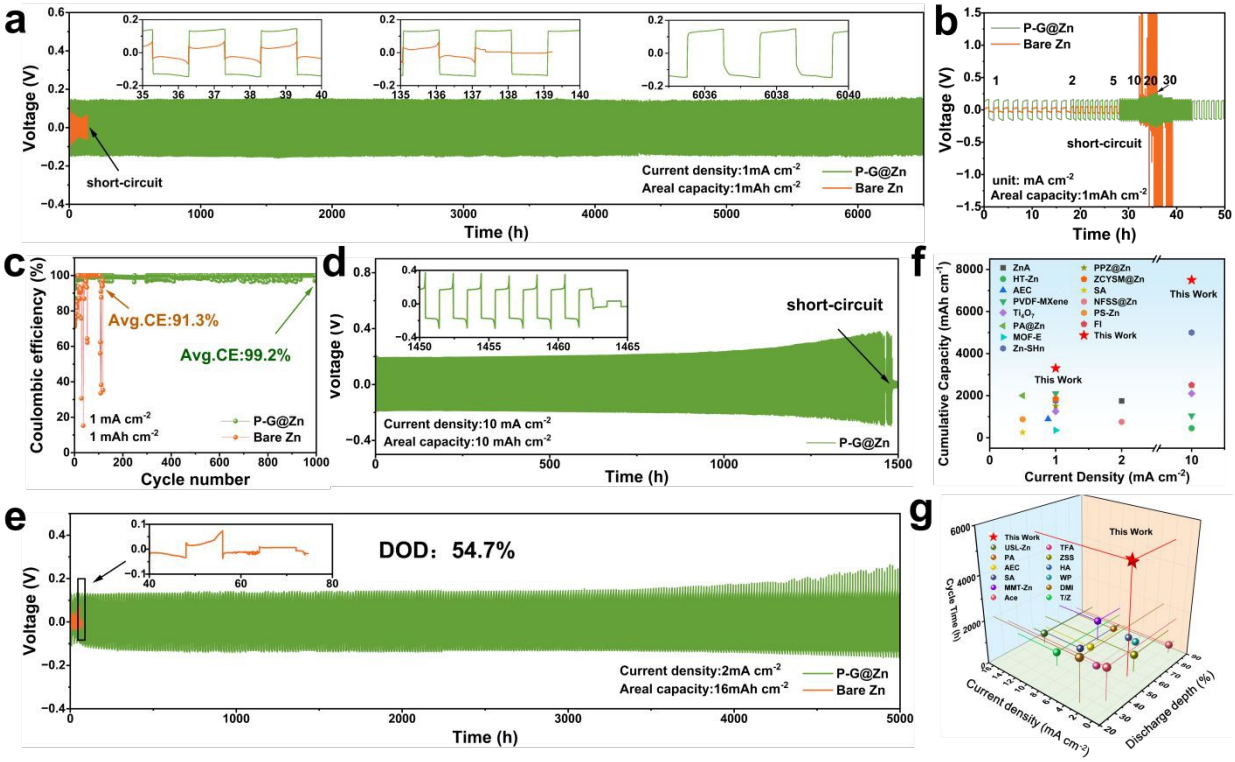

Fig. 5. Electrochemical stability and reversibility of Zn electrodes. (a) The long-term cycling performance of Zn||Zn symmetric cells at current density of 1 mA cm^{-2} and areal capacity of 1 mA h cm^{-2}. (b) Cycling performance of Zn||Zn symmetric cells various current densities at 1 mA h cm^{-2}. (c) Coulombic efficiencies Cu||Zn cells at current density of 1 mA cm^{-2} and areal capacity of 1 mA h cm^{-2}. (d) Cycling performance of P-G@Zn||P-G@Zn symmetric cells at current density of 10 mA·cm^{-2} and areal capacity of 10 mA h cm^{-2}. (e) Cycling performance of Zn||Zn symmetric cells at the Zn DOD of 54.7%. (f)and(g) Comparison of reversibly electrochemical performance of this work with recent reports focusing on AZIBs.

View Article Online
DOI: 10.1039/D5EE01408E

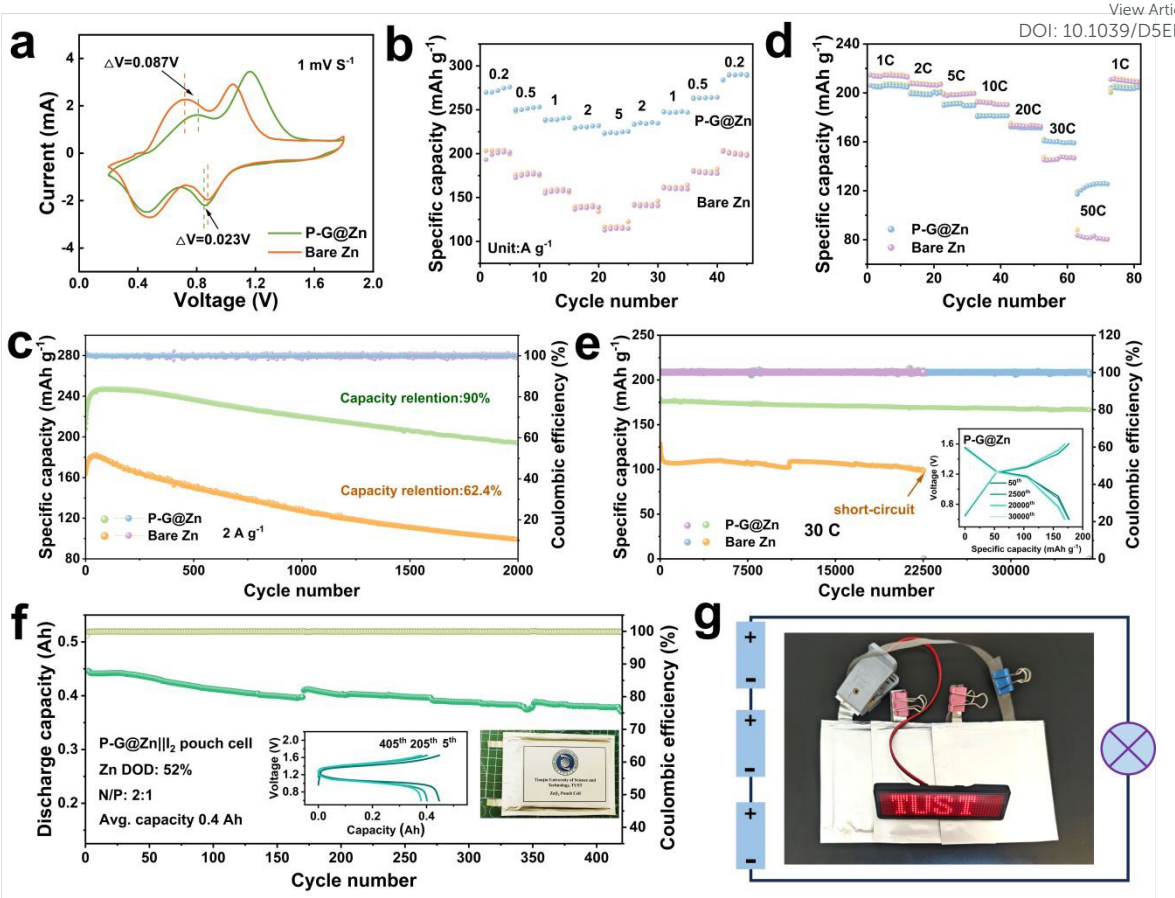

Fig. 6. Electrochemical behavior of Zn||V_2O_5 and Zn||I_2 full cells. (a) CV curves at a scan rate of 1 mV s^{-1} of Zn||V_2O_5 full cells. (b) Rate performance of Zn||V_2O_5 full cells. (c) Long-term cycling performances at current density of 2 A g^{-1}. (d) Rate performance of Zn||I_2 full cells. (e) Long-term cycling performances at current density of 30C. (f) Cycling performance of Zn||I_2 pouch cell at 1 A g^{-1}. (g) Optical image of typical electrical devices powered by Zn||I_2 pouch cells.

polarization in the Zn||V_2O_5 cell (**Fig. S41** and **S42**).[57] Furthermore, as shown in **Fig. 6b** and **S43**, the cell demonstrates excellent rate performance at increasing current densities, exhibiting superior stability and high reversibility compared to bare Zn.[58] Remarkably, the P-G@Zn||V_2O_5 full cell retains 90% of its capacity after 2000 cycles at a current density of 2 A·g^{-1}, significantly outperforming the bare Zn||V_2O_5 cell, which retains only 62.4% (**Fig. 6c**).

Similarly, the P-G@Zn||I_2 full cell exhibited superior kinetics and stability. As shown in **Fig. 6d**, the slope of the fitted curve for the P-G@Zn redox peaks in the CV curves at various scan rates surpasses that of bare Zn (**Fig. S44** and **S45**), indicating enhanced stability within the P-G SEI layer. This stability facilitates the fast migration of Zn^{2+} across the electrolyte and separator, thereby enabling exceptional electrochemical performance.[59-61] At a high current density of 30 C, the P-G@Zn||I_2 full cell retains an impressive capacity of 175 mAh g^{-1} after 36,000 cycles (**Fig. 6e**). In contrast, the bare Zn||I_2 cell maintains only 98.2 mAh g^{-1} after 20,000 cycles, corresponding to a retention rate of 95.4% (**Fig. S46**). To evaluate Zn||I_2 full-cell performance under practical conditions, we assembled soft-pack cells with high I_2 mass loading (15 mg cm^{-2}) using the P-G SEI layer fabricated via thermal spraying (**Fig. S47** and **S48**).[62-64] Notably, the ability to controllably and uniformly form the SEI layer represents a major bottleneck for scaling up the thermal spraying process. The pouch cell, with an area of 8 × 9 cm^2 and tested at a Zn DOD of 52%, delivered a high specific capacity of 341.85 mAh g^{-1} with 82.8% capacity retention after 400 cycles at 1 A g^{-1} (**Fig. 6f**). Additionally, **Fig. 6g** depicts three small-sized P-G@Zn||I_2 pouch cells powering over 50 light-emitting diodes requiring a working voltage of 3–4 V. These findings underscore the efficacy of the P-G SEI layer in stabilizing Zn electrodes, reducing side reactions, and enhancing redox reversibility, offering a promising strategy for the development of high-performance aqueous zinc batteries (**Fig. S49** and **S50**).

Conclusions

This study introduces a hybrid SEI layer with an ion-pumping effect as an innovative solution to enhance the reversibility and stability of zinc anodes, advancing the practical application of aqueous zinc-ion batteries (AZIBs). The P-G SEI layer suppresses corrosion and hydrogen evolution reactions while promoting uniform Zn^{2+} deposition, resulting in remarkable electrochemical performance. With a high Zn^{2+} transfer number of 0.77, fast desolvation kinetics, and exceptional cycling stability-lasting over 6500 hours in symmetrical cells and achieving ultra-long lifespans in full-cell

configurations- the P-G SEI layer demonstrates outstanding durability. Beyond symmetrical cells, it enables robust cycling in Zn||V_2O_5 and Zn||I_2 systems, including 36,000 cycles with 95.5% retention in Zn||I_2 coin cells and excellent performance in practical Zn||I_2 pouch cells. These findings highlight the P-G SEI layer as a transformative design for optimizing zinc anodes and advancing next-generation energy storage technologies.

Author contributions

L. Y., conceived the idea. Y. S., and X. L., carried out the materials synthesis and electrochemical characterization. Q. M., Z. R., N. X., and K. L., provided important experimental insights. L. J., J. L., Y. K., and L. T., reviewed and edited the manuscript. A. Y., and B. C., supervised the experiments and revised the content. All the authors discussed the results and contributed to writing the manuscript.

Conflicts of interest

There are no conflicts to declare.

Data availability

Data will be made available on request.

Acknowledgements

This work was supported by the National Natural Science Foundation of China (22208117), the fellowship of China Postdoctoral Science Foundation (2023M741818). The authors thank the synchrotron X–ray tomography measurement on BMIT-BM beamline at the Canadian Light Source. The authors also acknowledge the XPS and TOF-SIMS characterizations at the Vacuum Interconnected Nanotech Workstation (Nano-X), Suzhou Institute of Nano-Tech and Nano-Bionics, Chinese Academy of Sciences (Nano-X). The author also thanks the characterization of the Analytic and Testing Center of Tianjin University of Science and Technology and Na Yang for the molecular dynamic simulation. Leixin Yang, Yujie Shen, and Xintao Long contributed equally to this work.

References

1. C. Zhu, P. Li, G. Xu, H. Cheng and G. Gao, *Coordination Chemistry Reviews*, 2023, **485**, 215142.
2. Z. Peng, Z. Feng, X. Zhou, S. Li, X. Yin, Z. Zhang, N. Zhao, Z. He, L. Dai, L. Wang and C. Lu, *Journal of Energy Chemistry*, 2024, **91**, 345-369.
3. Q. Zhao, T. Xu, K. Liu, H. Du, M. Zhang, Y. Wang, L. Yang, H. Zhang, X. Wang and C. Si, *Energy Storage Materials*, 2024, **71**, 103605.
4. L. Tang, H. Peng, J. Kang, H. Chen, M. Zhang, Y. Liu, D. H. Kim, Y. Liu and Z. Lin, *Chemical Society Reviews*, 2024, **53**, 4877-4925.
5. X. Li, *Nature Energy*, 2025, **10**, 670-670.
6. M. Wu, Y. Zhang, L. Xu, C. Yang, M. Hong, M. Cui, B. C. Clifford, S. He, S. Jing, Y. Yao and L. Hu, *Matter*, 2022, **5**, 3402-3416.
7. C. Wang, X. Zeng, J. Qu, J. M. Cairney, Q. Meng, P. J. Cullen and Z. Pei, *Matter*, 2023, **6**, 3993-4012.
8. H. Peng, Y. Fang, J. Wang, P. Ruan, Y. Tang, B. Lu, X. Cao, S. Liang and J. Zhou, *Matter*, 2022, **5**, 4363-4378.
9. S. Wang, J. Li, B. Yang, B. Zhang, Z. Zhang, S. Zhou, Q. Wang, J. Ma and Z. Jin, *Nano Letters*, 2025, **25**, 5406-5414.
10. R. Zhao, J. Yang, X. Han, Y. Wang, Q. Ni, Z. Hu, C. Wu and Y. Bai, *Advanced Energy Materials*, 2023, **13**, 2203542.
11. B. Ren, S. Hu, A. Chen, X. Zhang, H. Wei, J. Jiang, G. Chen, C. Zhi, H. Li and Z. Liu, *Advanced Energy Materials*, 2024, **14**, 2302970.
12. R. Zhao, Y. Yang, G. Liu, R. Zhu, J. Huang, Z. Chen, Z. Gao, X. Chen and L. Qie, *Advanced Functional Materials*, 2021, **31**, 2001867.
13. K. Zhou, X. Yu, X. Dong, Z. Guo and Y. Wang, *Accounts of Chemical Research*, 2025, **58**, 599-611.
14. X. Cai, X. Wang, Z. Bie, Z. Jiao, Y. Li, W. Yan, H. J. Fan and W. Song, *Advanced Materials*, 2024, **36**, 2306734.
15. Y. Song, Y. Liu, S. Luo, Y. Yang, F. Chen, M. Wang, L. Guo, S. Chen and Z. Wei, *Advanced Functional Materials*, 2024, **34**, 2316070.
16. X. Cai, W. Tian, Z. Zhang, Y. Sun, L. Yang, H. Mu, C. Lian and H. Qiu, *Advanced Materials*, 2024, **36**, 2307727.
17. V. Aupama, J. Sangsawang, W. Kao-ian, S. Wannapaiboon, J. Pimoei, W. yoopensuk, M. Opchoei, Z. Tehrani, S. Margadonna and S. Kheawhom, *Electrochimica Acta*, 2024, **506**, 145059.
18. N. Yang, Y. Gao, F. Bu, Q. Cao, J. Yang, J. Cui, Y. Wang, J. Chen, X. Liu and C. Guan, *Advanced Materials*, 2024, **36**, 2312934.
19. R. Yao, Y. Zhao, L. Wang, C. Xiao, F. Kang, C. Zhi and C. Yang, *Energy & Environmental Science*, 2024, **17**, 3112-3122.
20. Sigel, A., Sigel, H., & Sigel, R. K. O. Springer. 2019, Vol. 16, pp. 485-556.
21. A. Xia, X. Pu, Y. Tao, H. Liu and Y. Wang, *Applied Surface Science*, 2019, **481**, 852-859.
22. J. G. Lyons, J. E. Kennedy, S. Lordan, L. M. Geever and C. L. Higginbotham, *Journal of Materials Science*, 2010, **45**, 3204-3214.
23. T. González, R. Castro-Muñoz, M. Vera, G. Merlet, L. Pino-Soto and R. Cabezas, *Journal of Industrial and Engineering Chemistry*, 2024, **135**, 67-86.
24. Z. Zhou, Y. Zhang, P. Chen, Y. Wu, H. Yang, H. Ding, Y. Zhang, Z. Wang, X. Du and N. Liu, *Chemical Engineering Science*, 2019, **194**, 142-147.
25. B. Luo, Y. Wang, S. Zheng, L. Sun, G. Duan, J. Lu, J. Huang and Z. Ye, *Energy Storage Materials*, 2022, **51**, 610-619.
26. J. Li, S. Zhou, X. Meng, Y. Chen, C. Fu, A. Azizi, X. Zhao, W. Xie, Z. Chang and A. Pan, *Science Bulletin*, 2023, **68**, 1283-1294.
27. W. Shi, Z. Song, W. Zhang, S. Lian, F. Huang, Q. An and Q. Li, *Energy & Environmental Science*, 2024, **17**, 7372-7381.
28. J. Wang, L. Jiao, Q. Liu, W. Xin, Y. Lei, T. Zhang, L. Yang, D. Shu, S. Yang, K. Li, C. Li, C. Yi, H. Bai, Y. Ma, H. Li, W. Zhang and B. Cheng, *Journal of Energy Chemistry*, 2024, **94**, 10-18.
29. W. Zhang, M. Dong, K. Jiang, D. Yang, X. Tan, S. Zhai, R. Feng, N. Chen, G. King, H. Zhang, H. Zeng, H. Li, M. Antonietti and Z. Li, *Nature Communications*, 2022, **13**, 5348.

30. L. Yang, Q. Ma, Y. Yin, D. Luo, Y. Shen, H. Dou, N. Zhu, R. Feng, Y. Kong, A. Yu, B. Cheng, X. Wang and Z. Chen, *Nano Energy*, 2023, **117**, 108799.
31. Z. Zhao, J. Zhao, Z. Hu, J. Li, J. Li, Y. Zhang, C. Wang and G. Cui, *Energy & Environmental Science*, 2019, **12**, 1938-1949.
32. K. Qiu, G. Ma, Y. Wang, M. Liu, M. Zhang, X. Li, X. Qu, W. Yuan, X. Nie and N. Zhang, *Advanced Functional Materials*, 2024, **34**, 2313358.
33. H. Du, R. Zhao, Y. Yang, Z. Liu, L. Qie and Y. Huang, *Angewandte Chemie International Edition*, 2022, **61**, e202114789.
34. Z. Shi, M. Li, X. Fu, Y. Zhang, S. Jiao and Y. Zhao, *Advanced Functional Materials*, 2024, **34**, 2316427.
35. C. Guo, J. Zhou, Y. Chen, H. Zhuang, J. Li, J. Huang, Y. Zhang, Y. Chen, S.-L. Li and Y.-Q. Lan, *Angewandte Chemie International Edition*, 2023, **62**, e202300125.
36. H. Dong, X. Hu, R. Liu, M. Ouyang, H. He, T. Wang, X. Gao, Y. Dai, W. Zhang, Y. Liu, Y. Zhou, D. J. L. Brett, I. P. Parkin, P. R. Shearing and G. He, *Angewandte Chemie International Edition*, 2023, **62**, e202311268.
37. M. Wu, X. Wang, F. Zhang, Q. Xiang, Y. Li and J. Guo, *Energy & Environmental Science*, 2024, **17**, 619-629.
38. T. Long, Q.-Y. Zhao, G.-Y. Yin, P.-X. Xie, S. Liu, X. Ma, Q. Wu, B.-Y. Lu, Z. Dai and X.-X. Zeng, *Advanced Functional Materials*, 2024, **34**, 2315539.
39. W. Chen, Y. Tan, C. Guo, X. Zhang, X. He, W. Kuang, H. Weng, H. Du, D. Huang, Y. Huang, J. Xu and H. He, *Journal of Colloid and Interface Science*, 2024, **669**, 104-116.
40. L. Yao, G. Wang, F. Zhang, X. Chi and Y. Liu, *Energy & Environmental Science*, 2023, **16**, 4432-4441.
41. X. Wang, Y. Ying, X. Li, S. Chen, G. Gao, H. Huang and L. Ma, *Energy & Environmental Science*, 2023, **16**, 4572-4583.
42. S. Huang, R. Tang, X. Liu, Y. Zhang, Y. Tang, Z. Wen, M. Ye, Y. Yang and C. C. Li, *Energy & Environmental Science*, 2024, **17**, 591-601.
43. Z. Zheng, S. Guo, M. Yan, Y. Luo and F. Cao, *Advanced Materials*, 2023, **35**, 2304667.
44. X. Wang, Y. Ying, X. Li, S. Chen, G. Gao, H. Huang and L. Ma, *Energy & Environmental Science*, 2024, **17**, 3228-3229.
45. Z. Shi, M. Yang, Y. Ren, Y. Wang, J. Guo, J. Yin, F. Lai, W. Zhang, S. Chen, H. N. Alshareef and T. Liu, *ACS Nano*, 2023, **17**, 21893-21904.
46. C. Chang, S. Hu, T. Li, F. Zeng, D. Wang, S. Guo, M. Xu, G. Liang, Y. Tang, H. Li, C. Han and H.-M. Cheng, *Energy & Environmental Science*, 2024, **17**, 680-694.
47. Z. Yang, F. Lai, Q. Mao, C. Liu, R. Wang, Z. Lu, T. Zhang and X. Liu, *Advanced Materials*, 2024, **36**, 2311637.
48. X. Yang, Q. Zhou, S. Wei, X. Guo, P. J. Chimtali, W. Xu, S. Chen, Y. Cao, P. Zhang, K. Zhu, H. Shou, Y. Wang, X. Wu, C. Wang and L. Song, *Small Methods*, 2024, **8**, 2301115.
49. B. Liu, C. Wei, Z. Zhu, Y. Fang, Z. Bian, X. Lei, Y. Zhou, C. Tang, Y. Qian and G. Wang, *Angewandte Chemie International Edition*, 2022, **61**, e202212780.
50. Q. Zhang, Y. Ma, Y. Lu, Y. Ni, L. Lin, Z. Hao, Z. Yan, Q. Zhao and J. Chen, *Journal of the American Chemical Society*, 2022, **144**, 18435-18443.
51. Q. Hu, J. Hou, Y. Liu, L. Li, Q. Ran, J. Mao, X. Liu, J. Zhao and H. Pang, *Advanced Materials*, 2023, **35**, 2303336.
52. Y. Guo, W. Cai, Y. Lin, Y. Zhang, S. Luo, K. Huang, H. Wu and Y. Zhang, *Energy Storage Materials*, 2022, **50**, 580-588.
53. J. Zhu, W. Deng, N. Yang, X. Xu, C. Huang, Y. Zhou, M. Zhang, X. Yuan, J. Hu, C. Li and R. Li, *Small*, 2022, **18**, 2202509.
54. R. Zhang, Y. Feng, Y. Ni, B. Zhong, M. Peng, T. Sun, S. Chen, H. Wang, Z. Tao and K. Zhang, *Angewandte Chemie International Edition*, 2023, **62**, e202304503.
55. J.-L. Yang, J. Li, J.-W. Zhao, K. Liu, P. Yang and H. J. Fan, *Advanced Materials*, 2022, **34**, 2202382.
56. G. Zhu, H. Zhang, J. Lu, Y. Hou, P. Liu, S. Dong, H. Pang and Y. Zhang, *Advanced Functional Materials*, 2024, **34**, 2305550.
57. Z. Wang, X. Zhu, X. Tao, P. Feng, J. Wang and J. Chen, *Advanced Functional Materials*, 2024, **34**, 2316223.
58. J. Duan, J. Dong, R. Cao, H. Yang, K. Fang, Y. Liu, Z. Shen, F. Li, R. Liu, H. Li and C. Chen, *Advanced Science*, 2023, **10**, 2303343.
59. D. Dong, T. Wang, Y. Sun, J. Fan and Y.-C. Lu, *Nature Sustainability*, 2023, **6**, 1474-1484.
60. S.-J. Zhang, J. Hao, H. Wu, C.-C. Kao, Q. Chen, C. Ye and S.-Z. Qiao, *ACS Nano*, 2024, **18**, 28557-28574.
61. L. Yang, D. Luo, Y. Zheng, T. Yang, Q. Ma, Y. Nie, H. Dou, Y. Zhang, R. Huang, A. Yu, L. Shui, X. Wang and Z. Chen, *Advanced Functional Materials*, 2022, **32**, 2204778.
62. X. Wang, J. Meng, X. Lin, Y. Yang, S. Zhou, Y. Wang and A. Pan, *Advanced Functional Materials*, 2021, **31**, 2106114.
63. S.-J. Zhang, J. Hao, H. Wu, Q. Chen, C. Ye and S.-Z. Qiao, *Advanced Materials*, 2024, **36**, 2404011.
64. H. Wu, J. Hao, S. Zhang, Y. Jiang, Y. Zhu, J. Liu, K. Davey and S.-Z. Qiao, *Journal of the American Chemical Society*, 2024, **146**, 16601-16608.

View Article Online
DOI: 10.1039/D5EE01408E

The data that support the findings of this study are available from the corresponding author upon reasonable request.